Computers and Fluids 226 (2021) 104989

Contents lists available at ScienceDirect

Computers and Fluids

journal homepage: www.elsevier.com/locate/compfluid

High-order accurate direct numerical simulation of flow over a MTU-T161 low pressure turbine blade

A.S. Iyer[a], Y. Abe[b], B.C. Vermeire[c], P. Bechlars[d], R.D. Baier[d], A. Jameson[e], F.D. Witherden[f], P.E. Vincent[a,*]

[a] Department of Aeronautics, Imperial College London, UK
[b] Institute of Fluid Science, Tohoku University, Japan
[c] Department of Mechanical, Industrial, and Aerospace Engineering, Concordia University, Canada
[d] MTU Aero Engines AG, Munich, Germany
[e] Department of Aerospace Engineering, Texas A&M University, USA
[f] Department of Ocean Engineering, Texas A&M University, USA

ARTICLE INFO

Article history:
Received 27 July 2020
Revised 29 March 2021
Accepted 23 April 2021
Available online 13 May 2021

Keywords:
Computational fluid dynamics
High-order methods
Direct numerical simulations
Low-Pressure turbines

ABSTRACT

Reynolds Averaged Navier-Stokes (RANS) simulations and wind tunnel testing have become the go-to tools for industrial design of Low-Pressure Turbine (LPT) blades. However, there is also an emerging interest in use of scale-resolving simulations, including Direct Numerical Simulations (DNS). These could generate insight and data to underpin development of improved RANS models for LPT design. Additionally, they could underpin a virtual LPT wind tunnel capability, that is cheaper, quicker, and more data-rich than experiments. The current study applies PyFR, a Python based Computational Fluid Dynamics (CFD) solver, to fifth-order accurate petascale DNS of compressible flow over a three-dimensional MTU-T161 LPT blade with diverging end walls at a Reynolds number of 200,000 on an unstructured mesh with over 11 billion degrees-of-freedom per equation. Various flow metrics, including isentropic Mach number distribution at mid-span, surface shear, and wake pressure losses are compared with available experimental data and found to be in agreement. Subsequently, a more detailed analysis of various flow features is presented. These include the separation/transition processes on both the suction and pressure sides of the blade, end-wall vortices, and wake evolution at various span-wise locations. The results, which constitute one of the largest and highest-fidelity CFD simulations ever conducted, demonstrate the potential of high-order accurate GPU-accelerated CFD as a tool for delivering industrial DNS of LPT blades.

1. Introduction

Commercial air transportation moved over 4.3 billion passengers in 2018 and produced upwards of 800 million tonnes of CO_2 and other Greenhouse Gases (GHG) [1,2]. The European Union and the United States have embarked on multi-billion dollar research projects to reduce the environmental impacts of aviation. For example, the renewed European Union Clean Sky 2 project [3] has the goal of developing and validating technology to enable a 75% reduction in CO_2 emissions and a 90% reduction in NO_X emissions by 2050 compared with 2000 levels.

Jet engine turbines extract energy from hot exhaust gasses that exit the combustion chamber of the engine, and use it to drive the compressor, fan, and other auxiliary systems. Turbine stages typically comprise approximately one-third of the total engine weight [4], with half of this contribution coming from the turbine blades. In order to reduce weight and CO_2 emissions, modern turbines are designed to use as few a blades as possible. However, this results in individual blades being subjected to higher-loading, which can lead to fully-separated flow over the aft-portion of each blade, and the introduction of complex, unsteady, three-dimensional flow phenomena. Taken together, these can have a detrimental effect on overall aerodynamic efficiency [5], which translates almost directly to an increase in specific fuel consumption [6], and GHG emissions. Therefore, there exists a trade-off between reducing the number of blades — and thus total turbine weight — while maintaining an appropriate level of aerodynamic performance.

At present, turbines are designed and optimised using a combination of RANS simulations [5,7], and wind tunnel testing [8–10]. However, RANS simulations have limited accuracy, espe-

* Corresponding author.
E-mail address: p.vincent@imperial.ac.uk (P.E. Vincent).

https://doi.org/10.1016/j.compfluid.2021.104989

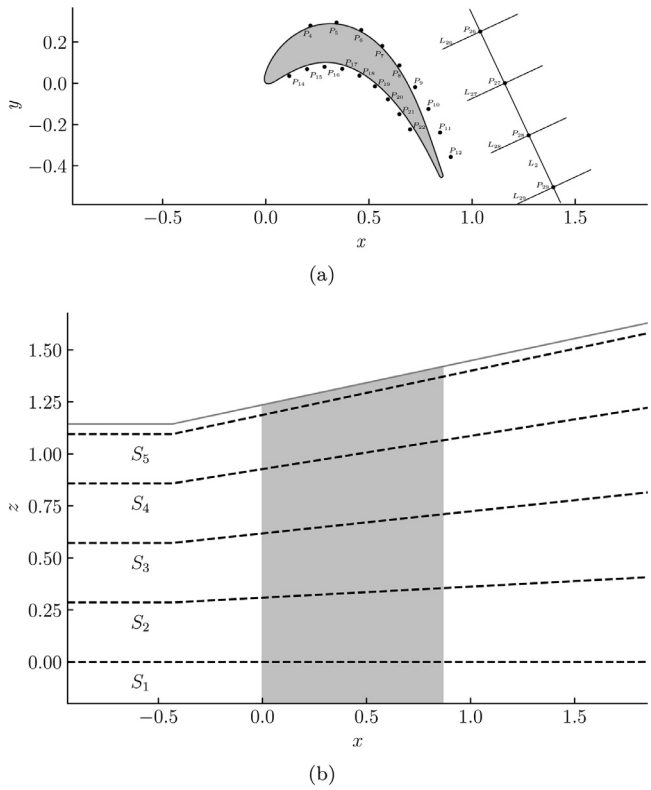

Fig. 1. Slice through the computational domain with constant $z = 0$ (a) showing the turbine blade profile, the location of points P_4 through P_{12}, P_{14} through P_{22} and P_{26} through P_{29}, and the location of lines L_2 and L_{26} through L_{29}. View of the computational domain in $x - z$ plane (b) showing the expanding end-wall profile, and the location of slices S_1 through S_5.

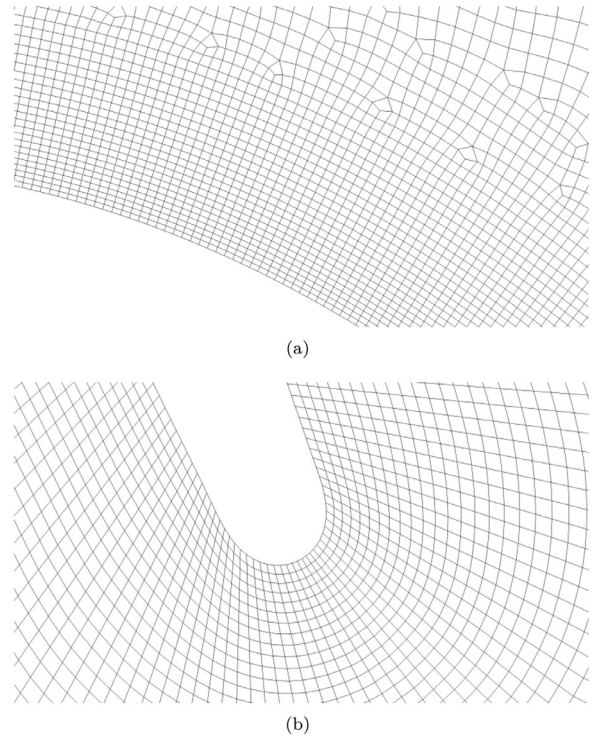

Fig. 2. Slices through computational mesh with constant $z = 0$ in the vicinity of the suction side (a) and trailing edge (b) of the turbine blade.

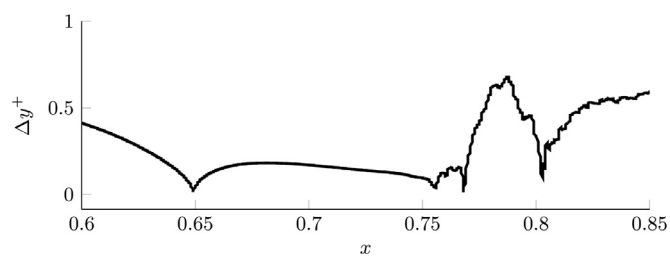

Fig. 3. Variation of Δy^+ along the suction side of the turbine blade.

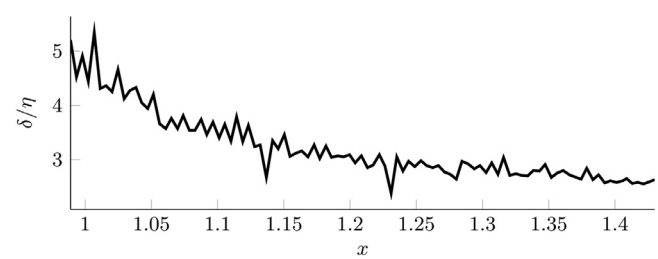

Fig. 4. Variation of δ/η along line L2 in the wake.

cially for unsteady flows, and experimental wind tunnel testing can be costly, time consuming, and only provides limited data. Consequently, there is an emerging interest in use of scale-resolving simulations, including Large Eddy Simulations (LES) [11–13] or Direct Numerical Simulations (DNS) [14,15]. Such simulations could generate insight and data to underpin development of improved RANS models for turbine design via *e.g.* direct analysis of the physics and/or machine learning based approaches. Additionally, they could underpin a virtual turbine wind tunnel capability, that is cheaper, quicker, and more data-rich than experiments, for characterising blade shapes and exploring the effect of modifications.

The current study applies PyFR [16,17], a Python based Computational Fluid Dynamics (CFD) solver, to fifth-order accurate petascale DNS of compressible flow over a three-dimensional MTU-T161 Low-Pressure Turbine (LPT) blade with diverging end walls at $Re = 200,000$ on an unstructured mesh with over 11 billion degrees-of-freedom per equation. This case is representative of general trends in modern turbine design, with fewer highly-loaded blades per stage. Section 2 details the adopted methodology and simulation setup, including the governing equations, domain, mesh, boundary conditions, and data extraction protocol. Section 3 details the results, including comparisons with available experimental data and a more detailed analysis of various flow features, including separation/transition on both the suction and pressure sides of the blade, end wall vortices, and wake evolution at various span-wise locations. Finally, Section 4 presents conclusions and directions for future work.

2. Methodology

2.1. Test case

In this study we undertake DNS of air flow over a highly loaded MTU-T161 turbine blade, bounded by diverging end walls. The configuration has been subject to an extensive experimental campaign, undertaken by MTU Aero Engines AG at a range of Reynolds and Mach numbers [9,10,18]. Here we consider a setup where the outflow isentropic Reynolds number based on the turbine blade chord is 200,000, and the outflow isentropic Mach number is 0.601.

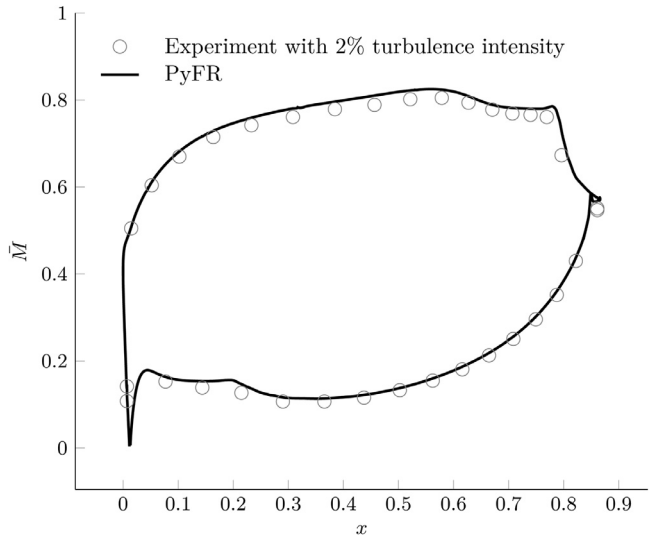

Fig. 5. Distribution of time-averaged isentropic Mach number $\tilde{M}$ over the pressure and suction sides of the turbine blade surface at mid-span obtained from PyFR and from the experiment with 2% turbulence intensity.

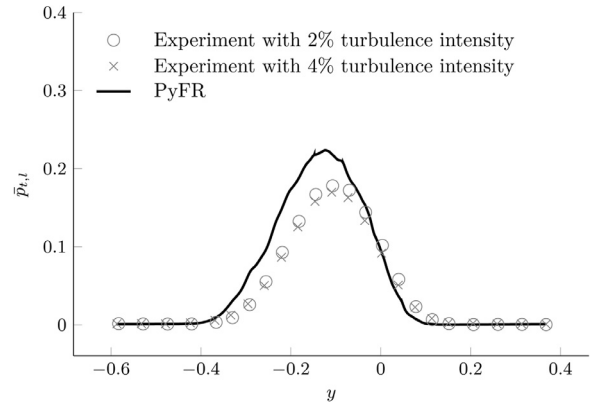

Fig. 7. Distribution of $\bar{p}_{t,l}$ along a line with constant $x = 1.206$ and $z = 0$ in the wake obtained from PyFR and from the experiments with 2% and 4% turbulence intensity. The numerical results are in agreement with the experimental data, capturing both the width of the wake and its shape. However, the predicted wake is slightly offset in the negative y direction relative to the experimental data, and the peak $\bar{p}_{t,l}$ is slightly over-predicted.

2.2. Governing equations

It was assumed that air behaves as a viscous ideal gas, governed by the compressible Navier-Stokes equations with constant viscosity, which can be written as

$$\frac{\partial \mathbf{u}}{\partial t} + \nabla \cdot \mathbf{f} = 0, \tag{1}$$

where $\mathbf{u} = \left\{\rho, \rho v_x, \rho v_y, \rho v_z, E\right\}^T$ is the solution, with ρ the fluid density, $\mathbf{v} = \{v_x, v_y, v_z\}^T$ the fluid velocity, and E the total energy of the fluid per unit volume, and where $\mathbf{f} = \mathbf{f}(\mathbf{u}, \nabla\mathbf{u}) = \mathbf{f}^i - \mathbf{f}^v$ is the flux, with

$$\mathbf{f}^i = \begin{Bmatrix} \rho v_x & \rho v_y & \rho v_z \\ \rho v_x^2 + p & \rho v_y v_x & \rho v_z v_x \\ \rho v_x v_y & \rho v_y^2 + p & \rho v_z v_y \\ \rho v_x v_z & \rho v_y v_z & \rho v_z^2 + p \\ v_x(E+p) & v_y(E+p) & v_z(E+p) \end{Bmatrix}, \tag{2}$$

where p is the pressure, which for an ideal gas is given by

$$p = (\gamma - 1)\left(E - \frac{1}{2}\rho\|\mathbf{v}\|^2\right), \tag{3}$$

with $\gamma = c_p/c_v$, where c_p and c_v are specific heat capacities at constant pressure and volume, respectively, and

$$\mathbf{f}^v = \begin{Bmatrix} 0 & 0 & 0 \\ \mathcal{S}_{xx} & \mathcal{S}_{yx} & \mathcal{S}_{zx} \\ \mathcal{S}_{xy} & \mathcal{S}_{yy} & \mathcal{S}_{zy} \\ \mathcal{S}_{xz} & \mathcal{S}_{yz} & \mathcal{S}_{zz} \\ v_i\mathcal{S}_{ix} + \Delta\partial_x T & v_i\mathcal{S}_{iy} + \Delta\partial_y T & v_i\mathcal{S}_{iz} + \Delta\partial_z T \end{Bmatrix}, \tag{4}$$

where

$$\mathcal{S}_{ij} = \mu(\partial_i v_j + \partial_j v_i) - \frac{2}{3}\mu\delta_{ij}\nabla \cdot \mathbf{v}, \tag{5}$$

with μ the dynamic viscosity, $\Delta = \mu c_p/Pr$, with Pr the Prandtl number, and T is the temperature, which for an ideal gas is given by

$$T = \frac{1}{c_v}\frac{1}{\gamma - 1}\frac{p}{\rho}. \tag{6}$$

In the current study values of $\gamma = 1.4$, $Pr = 0.71$, and $\mu = 2.7672 \times 10^{-6}$ were employed.

(a) (b)

Fig. 6. View of time-averaged wall shear LIC from PyFR (a) and oil-streak lines from the experiment with 2% turbulence intensity (b) on unwrapped surfaces of the turbine blade. The pressure surface is located on the bottom of each image, the suction surface is located on the top of each image, and the leading edge of the blade is located approximately half-way up each image.

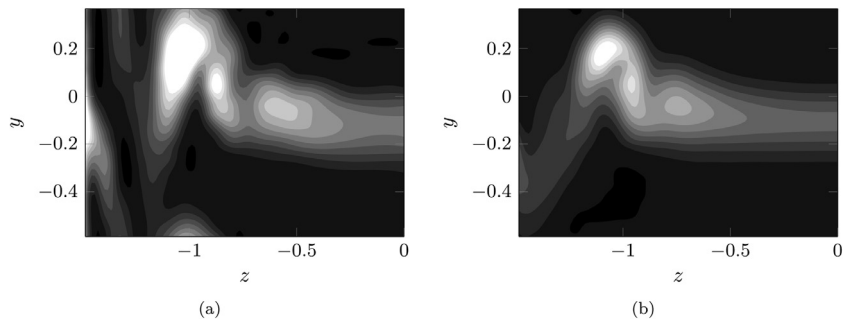

Fig. 8. Distributions of time-averaged total pressure loss $\bar{p}_{t,l}$ in the plane $x = 1.206$ with $z < 0$ from PyFR (a) and from the experiment with 2% turbulence intensity (b).

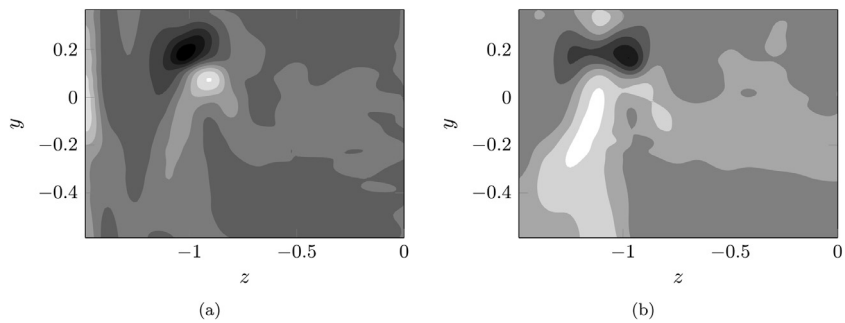

Fig. 9. Distributions of time-averaged stream-wise vorticity $\bar{\Gamma}$ in the plane $x = 1.206$ with $z < 0$ from PyFR (a) and from the experiment with 2% turbulence intensity (b).

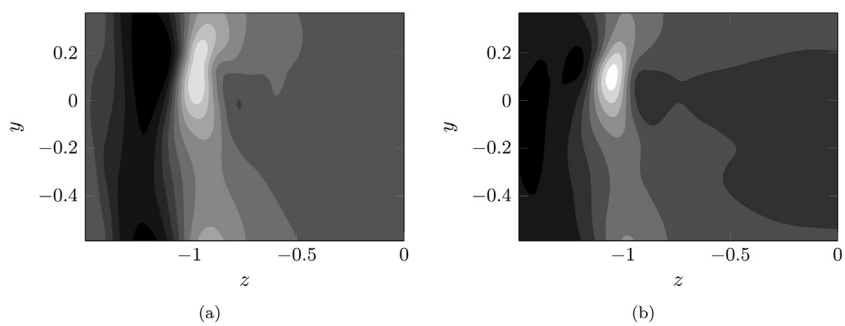

Fig. 10. Distributions of time-averaged flow angle from the x-axis $\bar{\Theta}$ in the plane $x = 1.206$ with $z < 0$ from PyFR (a) and from the experiment with 2% turbulence intensity (b).

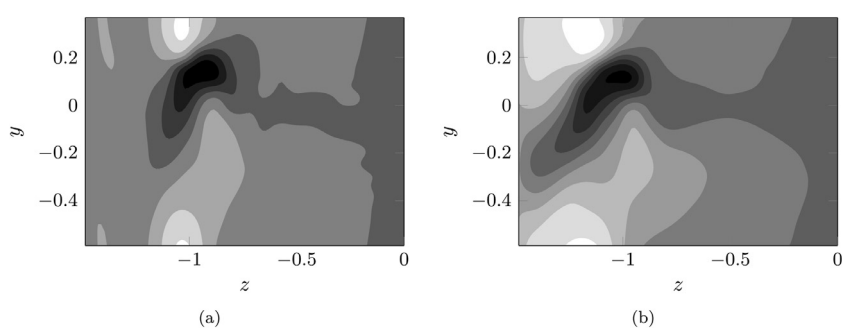

Fig. 11. Distributions of time-averaged flow angle from the z-axis $\bar{\Phi}$ in the plane $x = 1.206$ with $z < 0$ from PyFR (a) and from the experiment with 2% turbulence intensity (b).

2.3. Solver and numerical method

Simulations were undertaken on 5760 Nvidia K20X GPUs of the Titan supercomputer at Oak Ridge National Laboratory using PyFR [16,17], which is based on the high-order Flux Reconstruction approach of [19]. Discontinuous Galerkin flux correction functions were employed, a Rusanov Riemann solver was used to calculate the inter-element inviscid fluxes, the Local Discontinuous Galerkin (LDG) approach was used to calculate the inter-element viscous fluxes, an explicit RK45 scheme with adaptive time-stepping via a PI controller was employed to advance the solution in time, volume and surface flux anti-aliasing was applied to stabilise the solution, and all runs were performed using double precision arithmetic. Specifically, a patched version of PyFR v1.5.0 was employed. The patch is provided as Electronic Supplementary Material. Key functionality of PyFR v1.5.0 is summarised in Table 1.

Table 1
Key functionality of PyFR v1.5.0.

Dimensions	2D, 3D
Elements	Triangles, Quadrilaterals, Hexahedra, Tetrahedra, Prisms, Pyramids
Spatial Orders	Arbitrary
Time Steppers	Adaptive explicit Runge–Kutta schemes
Precisions	Single, Double
Platforms	CPUs, NVIDIA GPUs, AMD GPUs
Inter-Node Communication	MPI

2.4. Domain and mesh

The computational domain is shown in Fig. 1. The blade has a chord of 1.0, an axial chord of 0.8663, a pitch of 0.9557, and the domain has a span of 2.287 in the uniform span section. The origin of the domain is located at mid-span on the leading edge of the turbine blade. The inflow plane is located 0.92 upstream of the leading edge of the turbine blade. The outflow plane is located 1.86 downstream of the leading edge of the turbine blade.

Meshing was undertaken using Gmsh [20]. Regions of the mesh are shown in Fig. 2. A structured region of second-order-curved hexahedra, 23 elements deep, was located adjacent to the surface of the turbine blade and adjacent to the end walls. The remainder of the domain was meshed with second-order-curved unstructured hexahedra. Elements were sized to achieve DNS resolution throughout the domain. In total the mesh consisted of 90,760,192 elements, resulting in 11,345,024,000 degrees-of-freedom per equation when fourth-order polynomials were used to represent the solution within each element.

2.5. Boundary conditions

2.5.1. Inflow plane

At the inflow plane total temperature $T_{t,i}$, total pressure $p_{t,i}$, and inflow direction $\mathbf{n}_i$ were prescribed. Specifically, $T_{t,i}$ was chosen such that $c_pT_{t,i} = 3.5$ uniformly,

$$\begin{aligned} p_{t,i} = {} & p_i\left\{c_pT_{t,i}\Big/\left[c_pT_{t,i} - \frac{1}{2}\|u_i\|^2\left\{\tanh\left(\frac{\eta a_{bl}(h_z+z)}{\delta_{bl}}\right)^{n_{bl}}\right\}^{2/n_{bl}}\right]\right\}^{\gamma/(\gamma-1)} \\ & + p_i\left\{c_pT_{t,i}\Big/\left[c_pT_{t,i} - \frac{1}{2}\|u_i\|^2\left\{\tanh\left(\frac{\eta a_{bl}(h_z-z)}{\delta_{bl}}\right)^{n_{bl}}\right\}^{2/n_{bl}}\right]\right\}^{\gamma/(\gamma-1)} \\ & - p_i\left\{c_pT_{t,i}\Big/\left[c_pT_{t,i} - \frac{1}{2}\|u_i\|^2\right]\right\}^{\gamma/(\gamma-1)}, \end{aligned} \tag{7}$$

where $p_i = 0.9106$, $\|u_i\| = 0.4515$, $h_z = 1.14391$ and $\eta = 5.07514$, $a_{bl} = 0.33245$, $n_{bl} = 1.6667$, $\delta_{bl} = 0.2070$ were chosen to fit the resulting inflow velocity profile to available experimental data, and $\mathbf{n}_i = \{\cos(41^\circ), \sin(41^\circ), 0\}$. Note that the boundary condition is laminar, in the sense no turbulent fluctuations are injected.

2.5.2. Outflow plane

At the outflow plane a characteristic boundary condition was applied. As such a density $\rho_o = 0.8430$, velocity $\mathbf{v}_o = 0.6565\{\cos(-65^\circ), \sin(-65^\circ), 0\}$ and static pressure $p_o = 0.7910 + \delta p_o$ were prescribed, where $\delta p_o = 0.002285$. Note that due to the nature of the boundary condition p_o is not strictly enforced, and as such the empirical correction δp_o was applied in order to achieve the desired static pressure at the outflow plane.

2.5.3. Turbine blade surface and end walls

At the turbine blade surface and at the end walls an no-slip adiabatic boundary condition was applied.

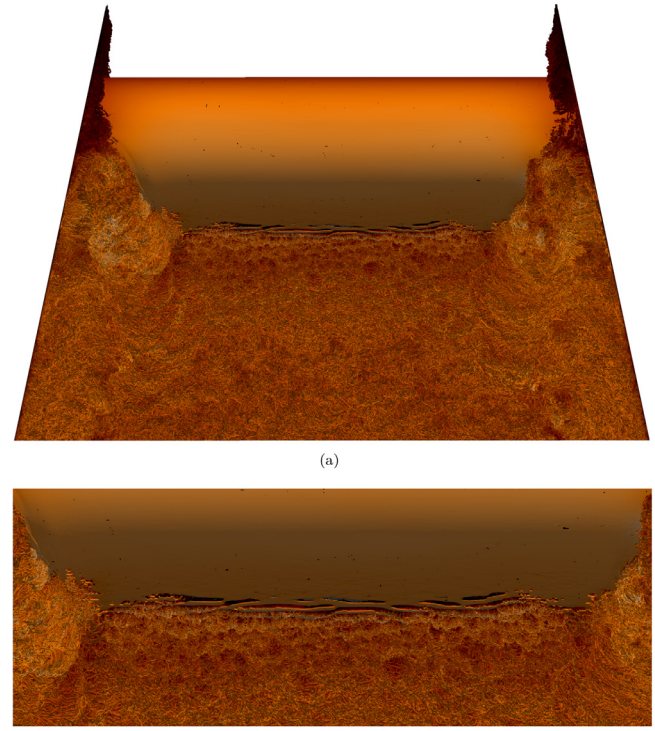

(a)

(b)

Fig. 12. Instantaneous snapshot of a Q-criteria iso-surface above the whole suction side of the turbine blade and in the wake (a) and above the region of the suction side where transition occurs (b).

2.5.4. Top and bottom

Periodic boundary conditions were applied to connect the top and bottom of the domain.

2.6. Startup process and data extraction protocols

2.6.1. Startup process

The simulation was initiated at $t = 0$ and advanced in time through to $t = 230.0$ via a series of partial-span-periodic and then full-domain runs, with second-order and then third-order polynomials used to represent the solution within each element of the mesh, and $p_o = 0.7910$ uniformly at the outflow plane. This was done to wash out large-scale initial transients.

The simulation was then restarted from the solution at $t = 230.0$, but with fourth-order polynomials used to represent the solution within each element of the mesh, and hence fifth-order accuracy in space, and $p_o = 0.7910 + \delta p_o$ uniformly at the outflow plane, where $\delta p_o = 0.002285$. This was run until $t = 240.0$ in order to achieve the experimentally observed static pressure at the outflow plane, and to wash out further transients, and then run until $t = 258.5$, during which time data was extracted for analysis. This latter period from $t = 240.0$ to $t = 258.5$ is henceforth referred to as the Data Extraction Period, and corresponds to approximately 11 flow passes over the turbine blade.

2.6.2. Solution snapshots

During the Data Extraction Period, solution snapshots containing instantaneous distributions of ρ, $\rho\mathbf{v}$, and E throughout the entire domain were obtained every 0.25 time units. These acted as restart checkpoint files, and allowed inspection of the full three-dimensional flow field. Snapshots containing instantaneous distributions of ρ, $\rho\mathbf{v}$, and E throughout the entire domain taken at $t = 240.0$ and $t = 258.5$ are available in a publicly accessible AWS S3 bucket with ARN `arn:aws:s3:::pyfr-mtu-t161-dns-data`.

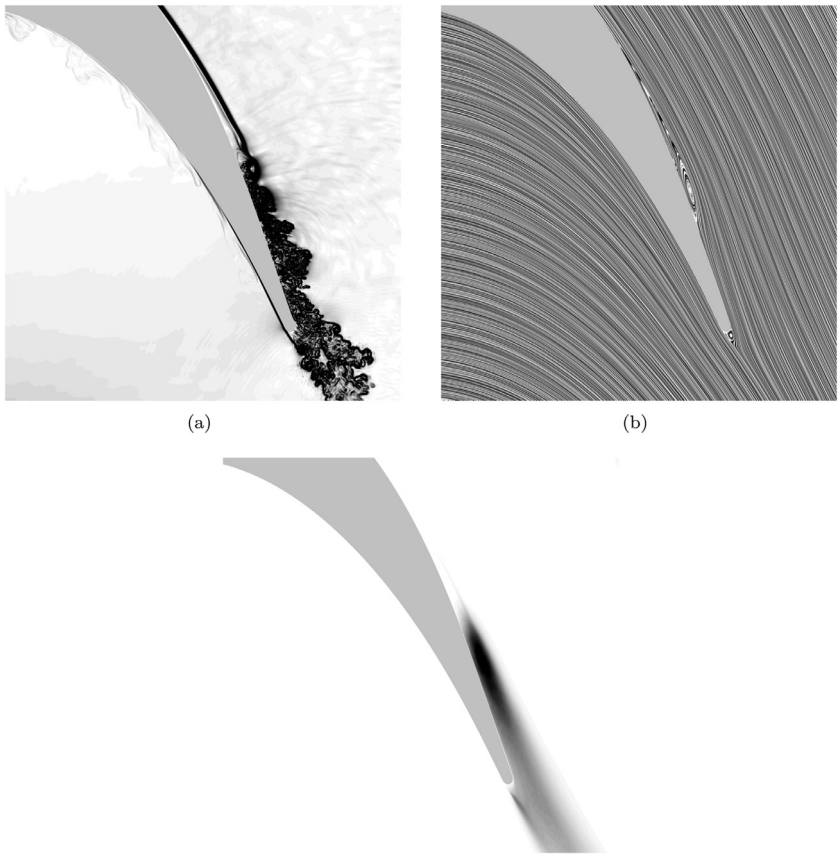

Fig. 13. Instantaneous snapshot of density gradient magnitude (a), LIC of the time averaged in-plane velocity (b) and turbulent kinetic energy E_{tk} (c) near the trailing edge of the suction side of the turbine blade.

2.6.3. Time-Averaging

During the Data Extraction Period various quantities were time-averaged throughout the entire domain, including:

1. $\overline{v_i}$ (3)
2. $\overline{\rho}$ (1)
3. $\overline{\rho v_i}$ (3)
4. $\overline{\rho v_i v_j}$ (6)
5. $\overline{\rho v_i v_j v_k}$ (10)
6. $\overline{p}$ (1)
7. $\overline{p v_i}$ (3)
8. $\overline{p v_i v_j}$ (6)
9. $\overline{p v_i v_j v_k}$ (10)
10. $\overline{p^2}$ (1)
11. $\overline{p^2 v_i}$ (3)
12. $\overline{p^2 v_i v_j}$ (6)
13. $\overline{p^3}$ (1)
14. $\overline{p^3 v_i}$ (3)
15. $\overline{p^4}$ (1)
16. $\overline{v_i v_j v_k v_l}$ (15)
17. $\overline{\sqrt{v_i v_i}}$ (1)
18. $\overline{\sqrt{\gamma p/\rho}}$ (1)
19. $\overline{\sqrt{\frac{v_i v_i}{\gamma p/\rho}}}$ (1)
20. $\overline{p\left(1+\frac{\gamma-1}{2}\frac{\rho v_i v_i}{\gamma p}\right)^{\frac{\gamma}{\gamma-1}}}$ (1)

where i, j, k, l each run through x, y, z, the numbers in parenthesis indicate the term count. Distributions of these time-averaged quantities are available in a publicly accessible AWS S3 bucket with ARN `arn:aws:s3:::pyfr-mtu-t161-dns-data`.

2.6.4. Point probes

During the Data Extraction Period, values of ρ, $\rho\mathbf{v}$, and E were obtained at 660 point locations every 30 time-steps. This data allowed spectra to be obtained. The time series of ρ, $\rho\mathbf{v}$, and E at each of the 660 point locations are available in a publicly accessible AWS S3 bucket with ARN `arn:aws:s3:::pyfr-mtu-t161-dns-data`.

3. Results

3.1. Resolution

3.1.1. Boundary layer resolution

Fig. 3 plots variation of $\Delta y^+ = \Delta y\sqrt{\overline{\rho}\,\overline{\tau}}/\mu$ along the suction side of the turbine blade surface, where Δy is the normal distance from the blade surface to the first solution point, $\overline{\rho}$ is the local time-averaged density, and $\overline{\tau}$ is the local time-averaged wall shear stress. $\Delta y^+ < 1$ at all locations. Hence, it is concluded that the mesh resolution is sufficient for DNS of the boundary layer [21].

3.1.2. Free-Stream resolution

An estimate of the Kolmogorov length scale η can be obtained at each point in the computational domain, as can the characteristic solution point spacing δ. Moving from the laminar flow region on the suction side of the turbine blade into the turbulent wake, the ratio δ/η is seen to grow monotonically, peaking

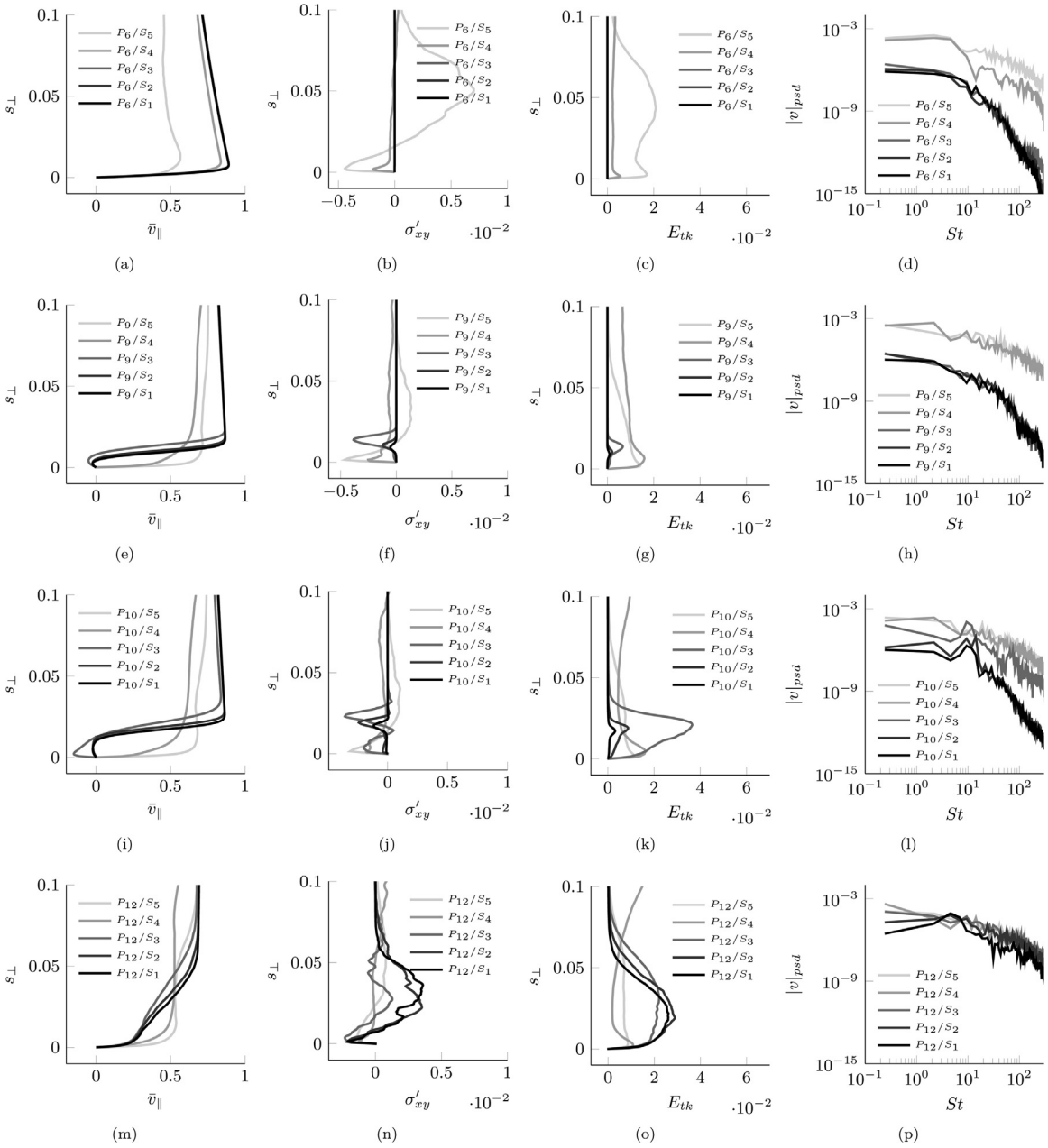

Fig. 14. Plots of time-averaged wall-parallel velocity $\bar{v}_\parallel$ as a function of wall-normal distance $s_\perp$ along lines P_i/S_j for $i = 6$ (a), $i = 9$ (e), $i = 10$ (i) and $i = 12$ (m), for various j. Plots of Favre averaged xy Reynolds stress σ'_{xy} as a function of wall-normal distance $s_\perp$ along lines P_i/S_j for $i = 6$ (b), $i = 9$ (f), $i = 10$ (j) and $i = 12$ (n), for various j. Plots of turbulent kinetic energy E_{tk} as a function of wall-normal distance $s_\perp$ along lines P_i/S_j for $i = 6$ (c), $i = 9$ (g), $i = 10$ (k) and $i = 12$ (o), for various j. Plots of velocity magnitude power spectral density $|v|_{psd}$ as a function of Strouhal number St at points P_i/S_j for $i = 6$ (d), $i = 9$ (h), $i = 10$ (l) and $i = 12$ (p), for various j. Note that line P_i/S_j resides in S_j, intersects the turbine blade surface normally in the x-y plane, and passes through the z-wise projection of point P_i onto slice S_j. Also note that point P_i/S_j is the z-wise projection of point P_i onto slice S_j.

at $\delta/\eta \approx 5$ and then decreasing along line L2 as per the plot in Fig. 4, asymptoting towards $\delta/\eta \approx 2$ in the far field. Based on previous results [22], $\delta/\eta \approx 5$ is sufficient for DNS resolution of first and second-order statistics. Hence, it is concluded that the mesh resolution is sufficient for DNS of the wake.

3.2. Validation

3.2.1. Blade surface

To validate the accuracy of our numerical simulations we compare our results against the experimental data of MTU Aero Engines. The distribution of time-averaged isentropic Mach number $\tilde{M}$ over the blade at the mid-span location is shown in Fig. 5. The DNS results achieve very good agreement with the experimental data at all measurement locations on both the pressure and suction sides of the blade. Furthermore, a comparison between the Line Integral Convolution (LIC) of time-averaged wall shear from the DNS results and experimental oil streak lines is shown in Fig. 6. On the suction side we observe that the DNS results accurately predict the turbulent end-wall effects and their development downstream on the suction side of the blade. Also, the location and curved shape of the mid-span separation line, which is demarcated by a horizontal edge in the oil streak lines ahead of the mid-chord, is also predicted accurately. Finally, we note that the behaviour on the pressure side of the blade is also qualitatively consistent with the experimental data.

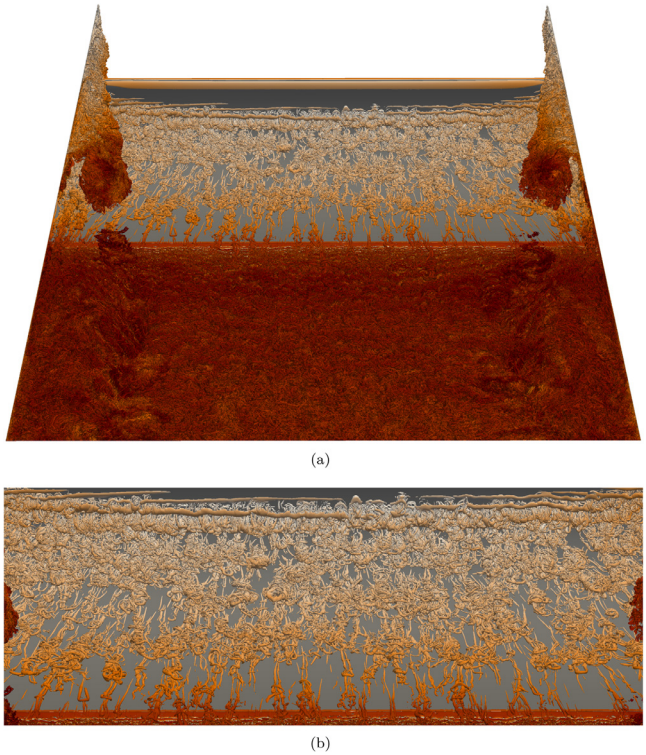

Fig. 15. Instantaneous snapshot of a Q-criteria iso-surface above the whole pressure side of the turbine blade and in the wake (a) and above the region of the pressure side where transition occurs (b).

3.2.2. Wake

Fig. 7 plots the time-averaged total pressure loss $\bar{p}_{t,l} = (\overline{p}_{t,i} - \bar{p}_t)/(\overline{p}_{t,i} - \overline{p}_o)$ along a line with constant $x = 1.206$ and $z = 0$ in the wake, where $\overline{p}_{t,i}$ is the time- and y-averaged total pressure at the inflow plane at $z = 0$, $\overline{p}_o$ is the time- and y-averaged pressure at the outflow plane at $z = 0$, and $\bar{p}_t$ is the time-averaged total pressure. The numerical results are in agreement with the experimental data, capturing both the width of the wake and its shape. However, the predicted wake is slightly offset in the negative y direction relative to the experimental data, and the peak total pressure loss is slightly over-predicted. This latter discrepancy is consistent with the laminar inlet conditions used in the current study, and their effect on bypass transition and subsequent wake formation.

Fig. 8 plots contours of $\bar{p}_{t,l}$ in the plane $x = 1.206$ with $z < 0$. The main features of the distribution are captured. However, the simulation results appear to exhibit a slightly larger and stronger end-wall vortex. This discrepancy is also consistent with the laminar inlet conditions used in the current study, which will cause over-thickening of the upstream boundary layer. Fig. 9 plots contours of time-averaged stream-wise vorticity $\bar{\Gamma} = (\bar{\Gamma}_x \cos(25^\circ) + \bar{\Gamma}_z \sin(25^\circ))/||u_i||$, where $\bar{\Gamma}_x$ and $\bar{\Gamma}_z$ are the time-averaged x and z vorticity, respectively. Figs. 10 and 11 plot contours of time-averaged flow angles $\bar{\Theta} = \arcsin(\bar{u}_x/|\bar{\mathbf{u}}|)$ and $\bar{\Phi} = \arcsin(\bar{u}_z/|\bar{\mathbf{u}}|)$ relative to the x- and z-axis, respectively, where $\bar{u}_x$ and $\bar{u}_z$ are the time-averaged x and z velocity, respectively, and $|\bar{\mathbf{u}}|$ is the time averaged velocity magnitude. Once again, the main features of the distributions are captured.

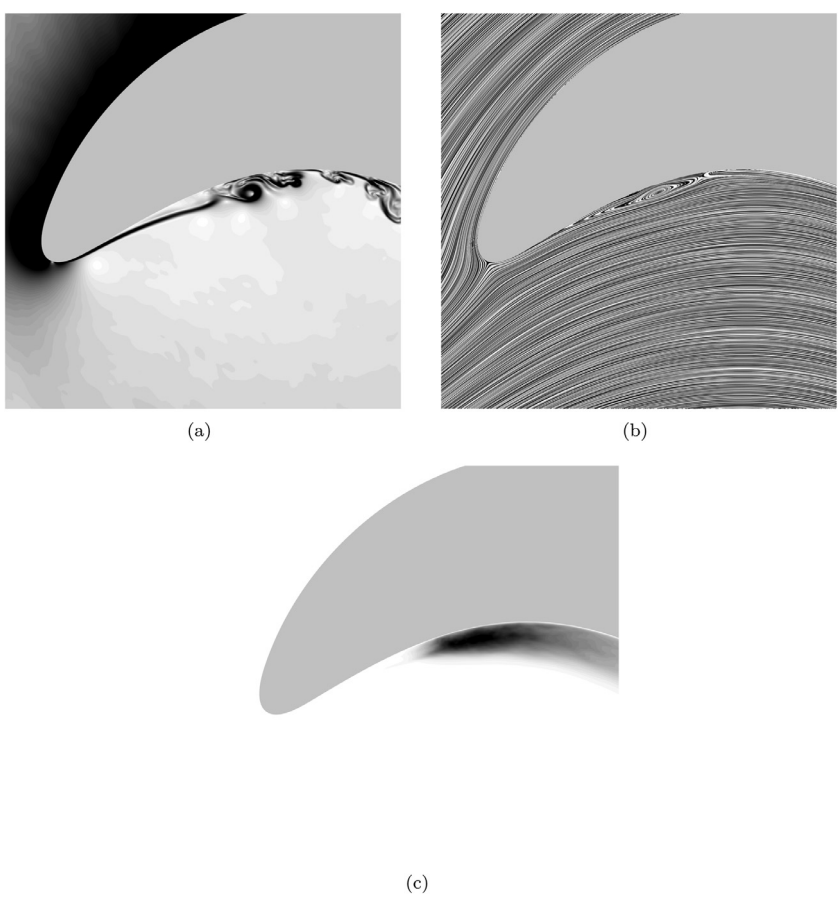

Fig. 16. Instantaneous snapshot of density gradient magnitude (a), LIC of the time averaged in-plane velocity (b) and turbulent kinetic energy E_{tk} (c) near the leading edge of the pressure side of the turbine blade.

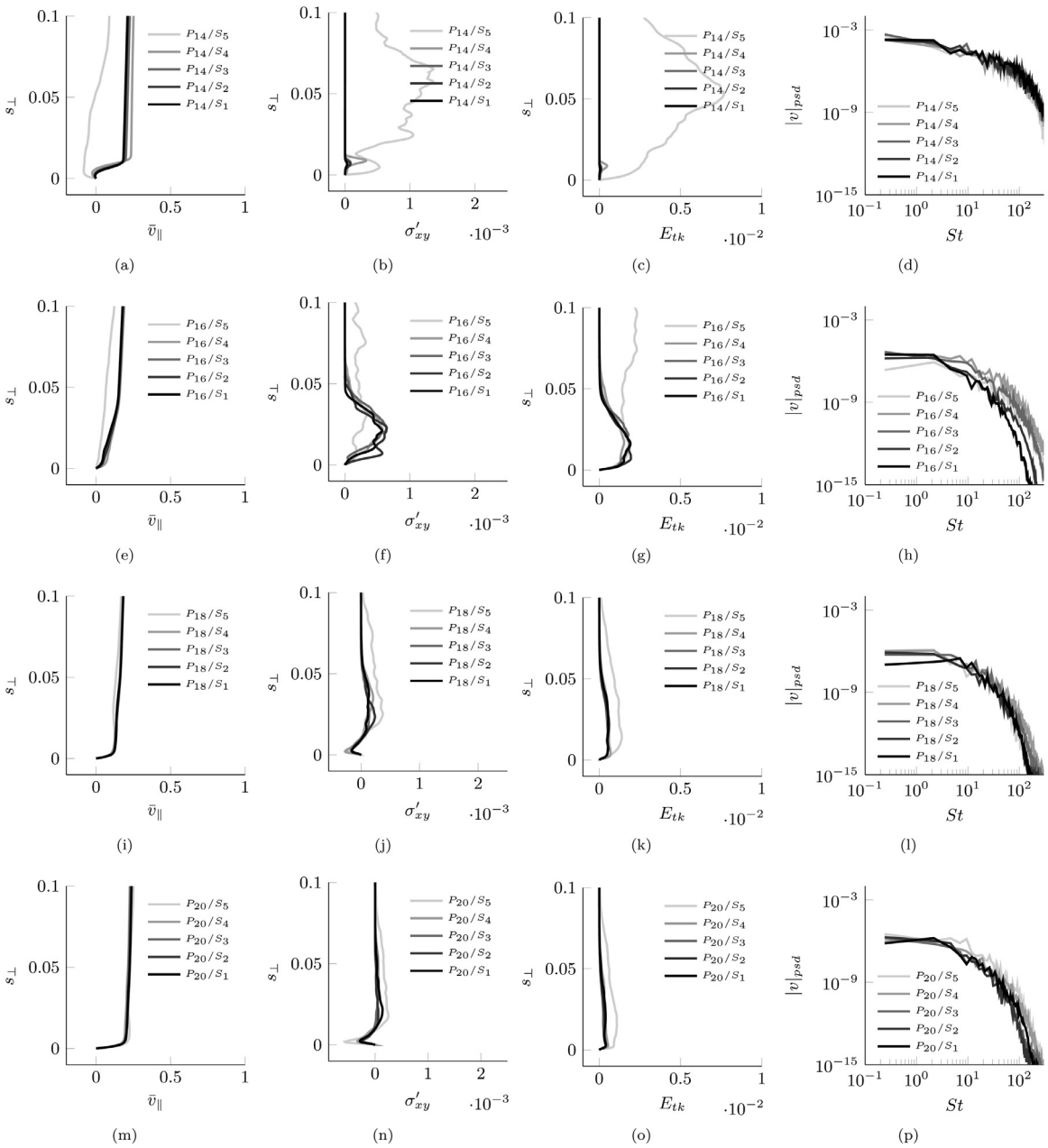

Fig. 17. Plots of time-averaged wall-parallel velocity $\bar{v}_\parallel$ as a function of wall-normal distance $s_\perp$ along lines P_i/S_j for $i = 14$ (a), $i = 16$ (e), $i = 18$ (i) and $i = 20$ (m), for various j. Plots of Favre averaged xy Reynolds stress σ'_{xy} as a function of wall-normal distance $s_\perp$ along lines P_i/S_j for $i = 14$ (b), $i = 16$ (f), $i = 18$ (j) and $i = 20$ (n), for various j. Plots of turbulent kinetic energy E_{tk} as a function of wall-normal distance $s_\perp$ along lines P_i/S_j for $i = 14$ (c), $i = 16$ (g), $i = 18$ (k) and $i = 20$ (o), for various j. Plots of velocity magnitude power spectral density $|v|_{psd}$ as a function of Strouhal number St at points P_i/S_j for $i = 14$ (d), $i = 16$ (h), $i = 18$ (l) and $i = 20$ (p), for various j. Note that line P_i/S_j resides in S_j, intersects the turbine blade surface normally in the x-y plane, and passes through the z-wise projection of point P_i onto slice S_j. Also note that point P_i/S_j is the z-wise projection of point P_i onto slice S_j.

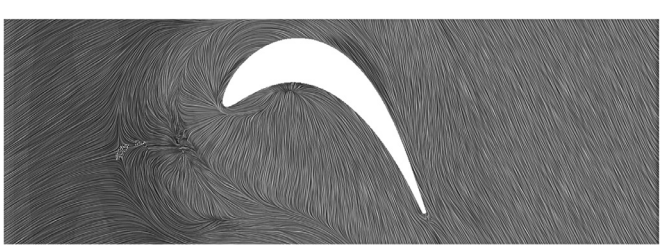

Fig. 18. LIC of time-averaged wall shear on one of the domain end-walls slack.

3.3. Physics

3.3.1. Suction-Side

Fig. 12 shows instantaneous snapshots of Q-Criterion iso-surfaces, which define vortical structures, over the suction-side of the turbine blade. It can be seen that turbulent transition in the mid-span region occurs near the aft portion of the blade. However, for the end-wall region transition occurs near the leading edge of the blade and propagates inwards towards the mid-span. This demonstrates that turbulent transition near the ends of the blade is dominated by end-wall effects, whereas turbulent transition in the mid-span region is relatively uniform across the span. The image also makes visually apparent the amount, and fidelity, of data

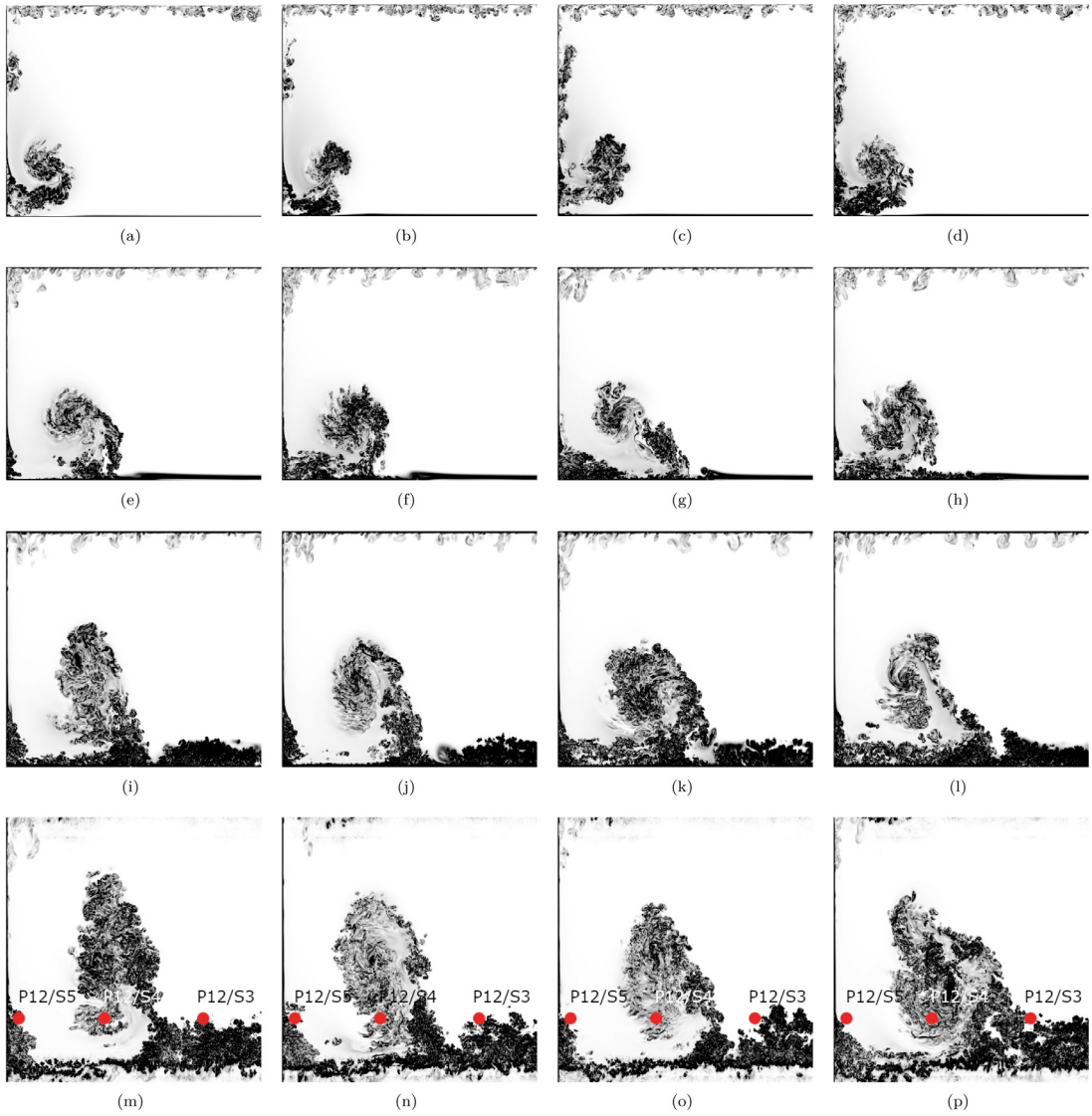

Fig. 19. Plots of vorticity magnitude near one of the end-walls in the plane $x = 0.343$ at $t = 247.0$ (a), $x = 0.343$ at $t = 247.5$ (b), $x = 0.343$ at $t = 248.0$ (c), $x = 0.343$ at $t = 248.5$ (d), $x = 0.648$ at $t = 247.0$ (e), $x = 0.648$ at $t = 247.5$ (f), $x = 0.648$ at $t = 248.0$ (g), $x = 0.648$ at $t = 248.5$ (h), $x = 0.788$ at $t = 247.0$ (i), $x = 0.788$ at $t = 247.5$ (j), $x = 0.788$ at $t = 248.0$ (k), $x = 0.788$ at $t = 248.5$ (l), $x = 0.897$ at $t = 247.0$ (m), $x = 0.897$ at $t = 247.5$ (n), $x = 0.897$ at $t = 248.0$ (o), $x = 0.897$ at $t = 248.5$ (p). The suction/pressure side of the turbine blade is at the bottom/top of each image, respectively. Points P_{12}/S_3, P_{12}/S_4, P_{12}/S_5, which are the z-wise projections of point P_{12} onto slices S_3, S_4 and S_5, respectively, are marked with red dots on (m) through (p). (For interpretation of the references to colour in this figure legend, the reader is referred to the web version of this article.)

made available by a DNS compared with *e.g.* wind tunnel experiments.

Fig. 13 shows a snapshot of the magnitude of the density gradient, an LIC of the time averaged in-plane velocity, and turbulent kinetic energy on a plane at the mid-span location of the blade. Similar to Figs. 12, 13 a shows that turbulent transition on the suction side occurs near the trailing edge aft of a Kelvin-Helmholtz instability. By comparing the density gradients in Fig. 13a and the time averaged velocity in Fig. 13b it can seen that transition actually occurs partway along a small closed laminar separation bubble. Fig. 13c shows that turbulent transition initiates in the shear layer between the outer edge of the laminar separation bubble and the mean flow. The turbulence intensity grows along this interface, rapidly amplifies in the aft portion of the separation bubble, and then propagates downstream as a turbulent wake.

Fig. 14 shows plots of time-averaged wall-parallel velocity $\bar{v}_{\parallel}$, Favre averaged xy Reynolds stress σ'_{xy}, and turbulent kinetic energy E_{tk} as a function of wall-normal distance $s_{\perp}$, at a total of 20 locations on the suction-side of the turbine blade, as well as the velocity power spectral density $|v|_{psd}$ as a function of Strouhal number

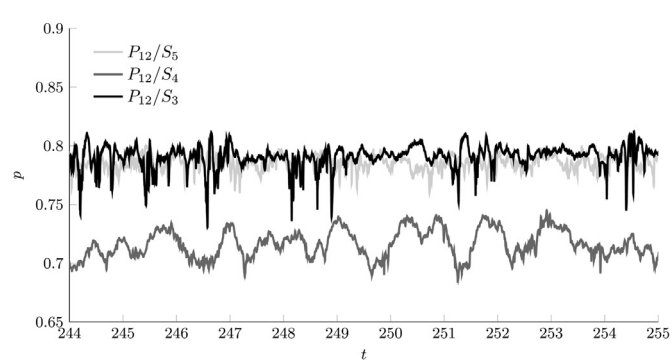

Fig. 20. Time history of static pressure p at points P_{12}/S_3, P_{12}/S_4, P_{12}/S_5, which are the z-wise projections of point P_{12} onto slices S_3, S_4 and S_5, respectively.

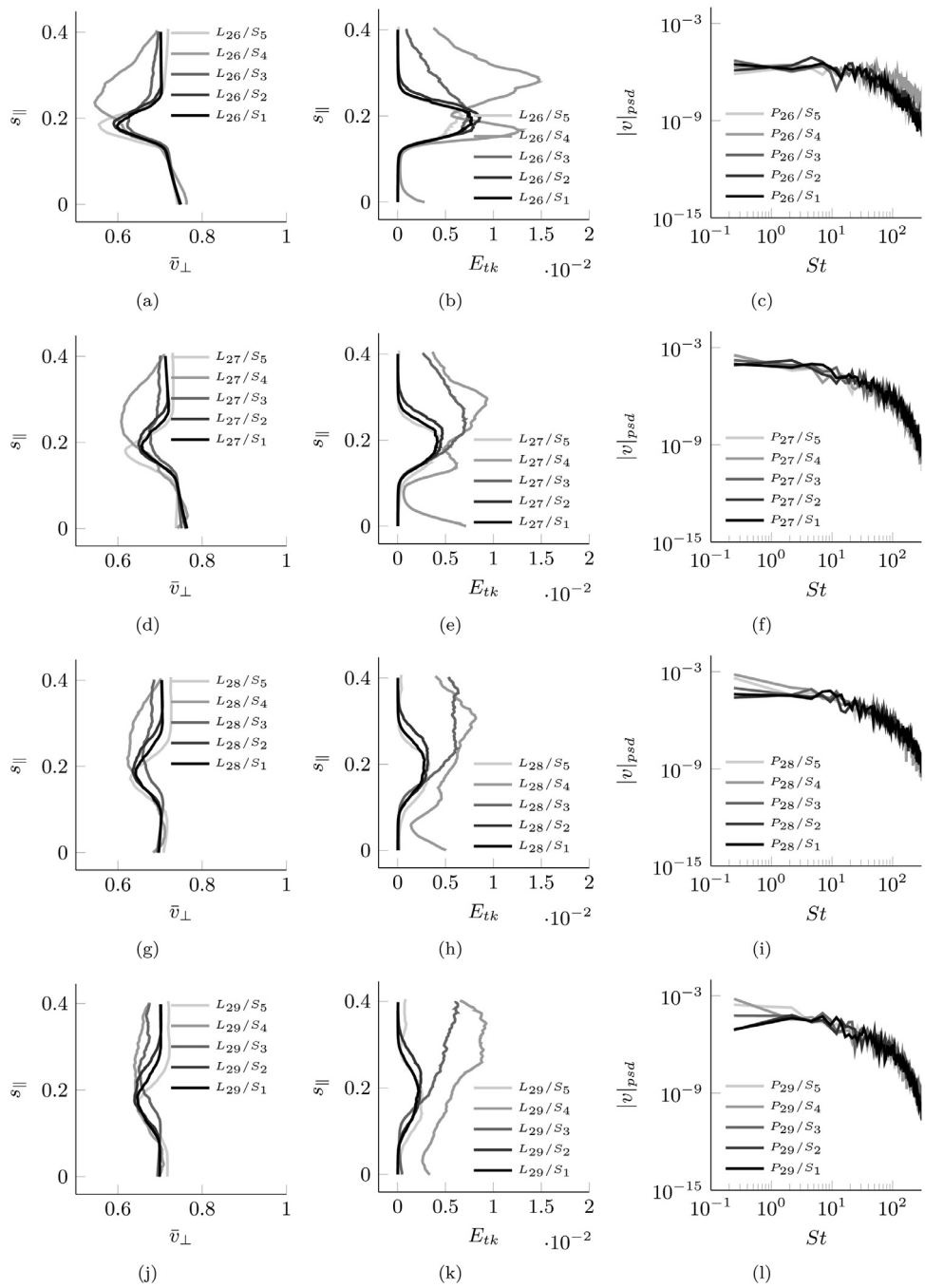

Fig. 21. Plots of time-averaged line-normal velocity $\bar{v}_\perp$ as a function of distance $s_\parallel$ along lines L_i/S_j for $i = 26$ (a), $i = 27$ (d), $i = 28$ (g) and $i = 29$ (j), for various j. Plots of turbulent kinetic energy E_{tk} as a function of wall-distance $s_\parallel$ along the lines P_i/S_j for $i = 26$ (b), $i = 27$ (e), $i = 28$ (h) and $i = 29$ (k), for various j. Plots of velocity magnitude power spectral density $|v|_{psd}$ as a function of Strouhal number St at points P_i/S_j for $i = 26$ (c), $i = 27$ (f), $i = 28$ (i) and $i = 29$ (l), for various j. Note that line L_i/S_j is the z-wise projection of line L_i onto slice S_j, and $s_\parallel$ is measured from the end of the line with the smallest x-coordinate. Also note that the point P_i/S_j is the z-wise projection of point P_i onto slice S_j.

St at the same locations. In the mid-span region flow is attached (Fig. 14a) and laminar (Fig. 14c/d) on the upstream part of the blade surface. Moving downstream, mid-span flow then separates (Fig. 14e) and transition begins near the inflection point of the velocity profile (Fig. 14g) driven by a Kelvin-Helmholtz instability. The mid-span separation bubble then grows in size and strength (Fig. 14i), and coherent structures from the Kelvin-Helmholtz instability become apparent (Fig. 14l) with a peak around $St = 10$. Finally, by the trailing edge of the blade, the mid-span flow reattaches (Fig. 14m) and a turbulent wake emerges (Fig. 14o/p). In the end-wall region flow is attached (Fig. 14a) and turbulent ((Fig. 14c/d) on the upstream part of the blade surface. Moving downstream in the end-wall region, wall-parallel flow remains persistently attached and turbulent at all stream-wise locations. Specifically, the turbulent kinetic energy starts off high (Fig. 14c) inside the region where end-wall vortices dominate, but then decreases moving downstream as these structures move away from the wall (Fig. 14k/o).

3.3.2. Pressure-side

Fig. 15 shows instantaneous snapshots of Q-Criterion isosurfaces, which define vortical structures, over the pressure-side

of the turbine blade. It can be seen that the flow is laminar at the leading edge on the pressure side of the blade. Slightly aft of the leading edge the flow undergoes turbulent transition, leading to the formation of a number of large coherent vortices. The location of this transition point correlates with a separation bubble shown in the shear LIC lines of Fig. 6. While some end-wall effects are visible, they are less pronounced than those on the suction side of the blade. The image also makes visually apparent the amount, and fidelity, of data made available by a DNS compared with *e.g.* wind tunnel experiments.

Fig. 16 shows a snapshot of the magnitude of the density gradient, an LIC of the time averaged in-plane velocity, and turbulent kinetic energy on a plane at the mid-span location of the blade. It can be seen that there is also a Kelvin-Helmholtz instability on the pressure side of the blade that forms around a small closed separation bubble. This instability initiates the formation of a number of large scale vortex structures inside the separation bubble, which are then propagated downstream inducing a pronounced increase in turbulent kinetic energy. These structures then gradually dissipate as they move downstream on the pressure side, which is apparent from a gradual decrease in turbulent kinetic energy moving towards the trailing edge of the blade.

Fig. 17 shows plots of time-averaged wall-parallel velocity $\bar{v}_{\parallel}$, Favre averaged *xy* Reynolds stress σ'_{xy}, and turbulent kinetic energy E_{tk} as a function of wall-normal distance $s_{\perp}$, at a total of 20 locations on the pressure-side of the turbine blade, as well as the velocity power spectral density $|v|_{psd}$ as a function of Strouhal number *St* at the same locations. The flow is separated at all span-wise locations near the leading edge of the blade (17 a). Turbulent transition occurs near the inflection point of the separated velocity profiles at all but the outermost span-wise location (17 c), leading to a rise in turbulent kinetic energy (17 g). Moving downstream the flow then reattaches to the blade at all span-wise locations (17 i), and remains attached over the remainder of the blade surface (17 m), while turbulent kinetic energy decreases monotonically. In general, the magnitude of the turbulent kinetic energy on the pressure side of the blade is significantly lower than that observed on the suction side.

3.3.3. End-wall

Fig. 18 shows an LIC of time-averaged wall shear stress on one of the domain end-walls. A bow-like structure upstream of the turbine blade is apparent where the LIC field lines converge along a curve. The area contained within this curve shows the extent of the end-wall vortex relative to the size of the turbine blade. In addition to the stagnation point directly at the leading edge of the blade, a secondary stagnation point is also apparent from convergence of the LIC field lines at a point situated upstream of the leading edge. This stagnation point forms due to impingement of the reversed flow in the end-wall vortex on the incoming free-stream velocity field. Additional secondary flow structures are also visible, including a stream-wise oriented structure underneath the pressure side of the blade.

Fig. 19 shows instantaneous snapshots of density gradient magnitude in various planes of constant *x* near one of the domain end-walls. Growth of the end-wall vortical structures in the stream-wise direction is apparent, as is their unsteady time-dependent nature.

Finally, Fig. 20 shows the time history of static pressure *p* recorded at points P_{12}/S_3, P_{12}/S_4, P_{12}/S_5, which are the *z*-wise projections of point P_{12} onto slices S_3, S_4 and S_5. The pressure at point P_{12}/S_4 is lower than that recorded at points P_{12}/S_3 and P_{12}/S_5. This is to be expected since as per Fig. 19m/n/o/p, P_{12}/S_4 is located within the end-wall vortex. Moreover, the pressure signal recorded at P_{12}/S_4 exhibits well defined low-frequency oscillations, indicating that the end-wall vortex undergoes quasi-periodic motions with approximately unit period. This latter result suggests that steady RANS approaches would fundamentally struggle to achieve accurate predictions in the end-wall region. However, given the separation of time-scales between the turbulence and the quasi-periodic motions, unsteady RANS approaches with a suitable model may be effective.

3.3.4. Wake

Fig. 21 shows plots of time-averaged line-normal velocity $\bar{v}_{\perp}$ and turbulent kinetic energy E_{tk} as a function of distance $s_{\parallel}$ along 20 lines in the wake of the turbine blade, as well as the velocity power spectral density $|v|_{psd}$ as a function of Strouhal number *St* at points on these lines. In the mid-span region a well defined compact wake structure is present directly behind the turbine blade (Fig. 21a), that weakens and broadens on moving downstream (Fig. 21d/g/j). In contrast, the end-wall regions exhibit a more complex structure. In particular, the wake within S_4, which cuts through the end-wall vortex, is displaced upwards from the mid-span wake (Fig. 21a/b), and one can also observe increased high-frequency power at this location (Fig. 21c).

4. Conclusions

The current study applied PyFR, a Python based Computational Fluid Dynamics (CFD) solver, to fifth-order accurate petascale DNS of compressible flow over a three-dimensional MTU-T161 LPT blade with diverging end walls at a Reynolds number of 200,000 on an unstructured mesh with over 11 billion degrees-of-freedom per equation. Various flow metrics, including isentropic Mach number distribution at mid-span, surface shear, and wake pressure losses were compared with available experimental data and found to be in agreement. Subsequently, a more detailed analysis of various flow features was presented. These included the separation/transition processes on both the suction and pressure sides of the blade, end-wall vortices, and wake evolution at various span-wise locations. The results, which constitute one of the largest and highest-fidelity CFD simulations ever conducted, demonstrate the potential of high-order accurate GPU-accelerated CFD as a tool for delivering industrial DNS of LPT blades. Such DNS could generate insight and data to underpin development of improved RANS models for LPT design via *e.g.* direct analysis of the physics or machine learning based approaches. Additionally, they could underpin a virtual LPT wind tunnel capability, that is cheaper, quicker, and more data-rich than experiments, for characterising blade shapes and exploring the effect of modifications. Future work should investigate the addition of further physics to the simulation setup, including Sutherland's law for temperature dependent viscosity, and the specification of fully turbulent inlet boundary conditions via e.g. a digital filter approach [23,24]. Future work should also explore using PyFR to simulate higher Mach number transonic cases, where shocks and shock-turbulence interactions are present. This will require implementation of specialised shock-capturing approaches [25–27].

Declaration of Competing Interest

The authors declare that they have no known competing financial interests or personal relationships that could have appeared to influence the work reported in this paper.

CRediT authorship contribution statement

A.S. Iyer: Writing - original draft, Writing - review & editing, Data curation, Methodology, Conceptualization. **Y. Abe:** Writing - original draft, Writing - review & editing, Data curation, Methodology, Conceptualization. **B.C. Vermeire:** Writing - original draft,

Writing - review & editing, Data curation, Methodology, Conceptualization. **P. Bechlars:** Writing - original draft, Writing - review & editing, Data curation, Methodology, Conceptualization. **R.D. Baier:** Writing - original draft, Writing - review & editing, Data curation, Methodology, Conceptualization. **A. Jameson:** Writing - original draft, Writing - review & editing, Data curation, Methodology, Conceptualization. **F.D. Witherden:** Writing - original draft, Writing - review & editing, Data curation, Methodology, Conceptualization. **P.E. Vincent:** Writing - original draft, Writing - review & editing, Data curation, Methodology, Conceptualization, Funding acquisition.

Acknowledgements

The authors are grateful for support from the Engineering and Physical Sciences Research Council (EP/K027379/1, EP/R030340/1), the European Commission (635962), the JSPS KAKENHI (19K15205), a Collaborative Research Project at the Institute of Fluid Science, Tohoku University, the Natural Sciences and Engineering Research Council of Canada (RGPAS-2017-507988, RGPIN-2017-06773), the Fonds de Recherche du Quebec - Nature et Technologies, and Air Force Office of Scientific Research under the oversight of Fariba Fahroo (FA9550-14-1-0186). An award of computer time was provided by the Innovative and Novel Computational Impact on Theory and Experiment (INCITE) program. This research used resources of the Oak Ridge Leadership Computing Facility at the Oak Ridge National Laboratory, which is supported by the Office of Science of the U.S. Department of Energy under Contract DE-AC05-00OR22725.

Supplementary material

Supplementary material associated with this article can be found, in the online version, at doi:10.1016/j.compfluid.2021.104989.

References

[1] . The world of air transport in 2018Tech. Rep. International Civil Aviation Organization; 2018.
[2] . Aviation benefits beyond borders - global fact sheetTech. Rep. International Air Transport Association; 2018.
[3] Council of European Union. Council regulation (EU) no 71/2008: establishing the clean sky 2 joint undertaking. 2014.
[4] Curtis EM, Hodson HP, Banieghbal MR, Denton JD, Howell RJ, Harvey NW. Development of blade profiles for low-pressure turbine applications. J Turbomach 1997;119(3):531–8.
[5] Tucker PG. Computation of unsteady turbomachinery flows: Part 1 - progress and challenges. Prog Aerosp Sci 2011;47(7):522–45. doi:10.1016/j.paerosci.2011.06.004.
[6] Gier J, Franke M, Hubner N, Schroder T. Designing low pressure turbines for optimized airfoil lift. J Turbomach 2010;132(3):12.
[7] . The effects of turbulence length scale on turbulence and transition prediction in turbomachinery flowsvol. 2B: Turbomachinery of Turbo Expo: Power for Land, Sea, and Air; 2014.
[8] . A test case for the numerical investigation of wake passing effects on a highly loaded LP turbine cascade bladevolume 1: Aircraft Engine; Marine; Turbomachinery; Microturbines and Small Turbomachinery of Turbo Expo: Power for Land, Sea, and Air; 2001.
[9] Martinstetter M. Experimentelle untersuchungen zur aerodynamik hoch belasteter niederdruckturbinen-beschaufelungen. Universitat der Bundeswehr Munchen; 2009.
[10] . Passive boundary layer control on a highly loaded low pressure turbine cascadevolume 7: Turbomachinery, Parts A, B, and C of Turbo Expo: Power for Land, Sea, and Air; 2010.
[11] Tucker PG. Computation of unsteady turbomachinery flows: Part 2 - LES and hybrids. Prog Aerosp Sci 2011;47(7):546–69.
[12] Michelassi V, Wissink J, Rodi W. Analysis of DNS and LES of flow in a low pressure turbine cascade with incoming wakes and comparison with experiments. Flow Turbul Combust 2002;69:295–329.
[13] . The effect of turbulent scales on low-pressure turbine aerodynamics: Part B - scale resolving simulationsvolume 2B: Turbomachinery of Turbo Expo: Power for Land, Sea, and Air; 2018.
[14] Müller-Schindewolffs C, Baier RD, Seume JR, Herbst F. Direct numerical simulation based analysis of RANS predictions of a low-pressure turbine cascade. J Turbomach 2017;139(8).
[15] Vincent PE, Witherden FD, Vermeire BC, Park JS, Iyer A. Towards green aviation with python at petascale. In: Proceedings of the international conference for high performance computing, networking, storage and analysis, SC'16. IEEE Press; 2016. ISBN 9781467388153
[16] Witherden FD, Farrington AM, Vincent PE. PyFR: an open source framework for solving advection–diffusion type problems on streaming architectures using the flux reconstruction approach. Comput Phys Commun 2014;185(11):3028–40.
[17] Witherden FD, Vermeire BC, Vincent PE. Heterogeneous computing on mixed unstructured grids with PyFR. Comput Fluids 2015;120:173–86.
[18] Gier J, Raab I, Schroder T, Hubner N, Franke M, Kennepohl F, Lippl F, Germain T. Preparation of aero technology for new generation aircraft engine LP turbines. In: European air and space conference, vol. CEAS-2007-139; 2007.
[19] Huynh HT. A flux reconstruction approach to high-order schemes including discontinuous Galerkin methods. In: Proceedings of 18th AIAA computational fluid dynamics conference, Miami, Florida; 2007. AIAA 2007-4079
[20] Geuzaine C, Remacle J-F. Gmsh: a 3-D finite element mesh generator with built-in pre- and post-processing facilities. Int J Numer Methods Eng 2009;79(11):1309–31. doi:10.1002/nme.2579.
[21] Nicholas JG, Rizzetta DP, Fureby C. Large-Eddy simulation: current capabilities, recommended practices, and future research. AIAA J 2010;48.
[22] Laizet S, Nedic J, Vassilicos C. Influence of the spatial resolution on fine-scale features in DNS of turbulence generated by a single square grid. Int J Comut Fluid Dyn 2015;29(3–5):286–302.
[23] Touber E, Sandham ND. Large-eddy simulation of low-frequency unsteadiness in a turbulent shock-induced separation bubble. Theor Comput Fluid Dyn 2009;23(2):79–107.
[24] Xie ZT, Castro IP. Efficient generation of inflow conditions for large eddy simulation of street-scale flows. Flow Turbul Combust 2008;81(3):449–70.
[25] Persson P, Peraire J. Sub-cell shock capturing for discontinuous Galerkin methods. AIAA Paper 2006-112; 2006.
[26] Barter GE, Darmofal DL. Shock capturing with higher-order PDE-based artificial viscosity. AIAA Paper 2007-3823; 2007.
[27] Trojak W, Dzanic T, Witherden FD. Shock capturing methods in high-order flux reconstruction I: graph viscosity and convex limiting approaches. AIAA Paper 2021-0496; 2021.